

The dusty environment of quasars . Far-IR properties of Optical Quasars ¹

Paola Andreani¹

INAF - Osservatorio Astronomico Padova, Vicolo dell'Osservatorio 5, Padova, I-35122, Italy, e-mail:andreani@pd.astro.it

Stefano Cristiani²

INAF - Osservatorio Astronomico di Trieste, Via G.B.Tiepolo 11 - I 34131 Trieste, Italy, e-mail:cristiani@ts.astro.it

Andrea Grazian³

Dipartimento di Astronomia, Università di Padova, Vicolo dell'Osservatorio 2, Padova, I-35122, Italy

Fabio La Franca

Dipartimento di Fisica, Università degli Studi "Roma Tre", viale della Vasca Navale 84, I-00146 Roma, Italy, e-mail:lafranca@fis.uniroma3.it

Pippa Goldschmidt

Astrophysics Group, Blackett Laboratory, Imperial College of Science Technology and Medicine, Prince Consort Road, London SW7 2BZ, UK

ABSTRACT

We present the ISO far-IR photometry of a complete sub-sample of optically selected bright quasars belonging to two complete surveys selected through multicolour (U,B,V,R,I) techniques. The ISOPHOT camera on board of the ISO Satellite was used to target these quasars at wavelengths of 7.3, 11.5, 60, 100 and

¹Max-Planck I. für Extraterrestrische Physik, Postfach 1312, 85741 Garching, Germany, e-mail:andreani@mpe.mpg.de

²Space Telescope - European Coordinating Facility European Southern Observatory, K. Schwarzschild str.2, D-85748 Garching, Germany, e-mail:cristia@eso.org

³European Southern Observatory, K. Schwarzschild str.2, D-85748 Garching, Germany, agrazian@eso.org

160 μm . Almost two thirds of the objects were detected at least in one ISOPHOT band. The detection rate is independent of the source redshift, very likely due to the negative K-correction of the far-IR thermal emission. More than a half of the optically selected QSOs show significant emission between 4 and 100 μm in the quasar rest-frame.

These fluxes have a very likely thermal origin, although in a few objects an additional contribution from a non-thermal component is plausible in the long wavelength bands. In a colour-colour diagram these objects span a wide range of properties from AGN-dominated to ULIRG-like. The far-IR composite spectrum of the quasar population presents a broad far-IR bump between 10 and 30 μm and a sharp drop at $\lambda > 100 \mu m$ in the quasar restframe. The amount of energy emitted in the far-IR, is on average a few times larger than that emitted in the blue and the ratio $\frac{L_{FIR}}{L_B}$ increases with the bolometric luminosity. Objects with fainter blue magnitudes have larger ratios between the far-IR ($\lambda > 60 \mu m$) fluxes and the blue band flux, which is attributed to extinction by dust around the central source. No relation between the blue absolute magnitude and the dust colour temperature is seen, suggesting that the dominant source of FIR energy could be linked to a concurrent starburst rather than to gravitational energy produced by the central engine.

Subject headings: AGN - active galaxies: ISM, photometry - ISM: dust, extinction, - Quasars: general - continuum - infrared: galaxies

1. Introduction

The properties of the circumnuclear environment are a key element to understand the formation and evolution of AGN. In particular, while these properties are well studied in the UV/optical spectral domain their mid-IR and far-IR characteristics are still a matter of debate.

The sampling of the far-IR part of the Spectral Energy Distribution (SED) is important for determining not only the overall energy balance but also to discriminate the dominant emitting mechanism and to trace any evolutionary path from a dust-enshrouded phase to a

¹based on observations with ISO, an ESA project with instruments funded by ESA Member States (especially the PI countries: France, Germany, the Netherlands and the United Kingdom) with the participation of ISAS and NASA

dust-free *regime*, corresponding to a "neat" optical phase (Sanders et al., 1989). Possibly related is the investigation of the structure and anisotropy of the obscuring-reprocessing torus as predicted by unification models of AGN. In particular, knowledge of the spectral region where the dust emission peaks and starts to become optically thick is needed to constrain the nature of the torus and its fundamental geometrical and physical parameters (dimensions, dust temperature and optical depth) providing an orientation-independent parameter to test the unification hypothesis.

IRAS observations have offered the first glimpse to the far-IR properties of optical quasars but did not have the required sensitivity to yield an unbiased view of the AGN class as a whole. In fact, only known optical quasars (PG quasars), with a very narrow range of fluxes and consequently a narrow range of luminosities at any given redshift, have been targeted and studied. The lack of any statistically well-defined sample prevented from any inference on the general FIR properties of *optically-selected quasars*. Also subsequent studies, based on *mm* emission of IRAS QSOs and of high-*z* optical QSOs (Chini et al., 1989, Omont et al. 1996, Andreani et al., 1999, Carilli et al., 2000, Omont et al., 2001, and references therein) and on ISO observations (Haas et al., 1998, 2000; Polletta et al., 2000; Oyabu et al., 2001), could not address this issue and mainly focussed on the question of the emitting mechanism.

The sampling of the shortest and longest parts of the IR spectrum via ISO observations is a key test to disentangle the emitting mechanism. However a typical conclusion of ISO studies is that it is not easy to disentangle pure AGN emission from a likely common FIR-emitting star-formation component. There is not a general agreement among different observations (Haas et al., 1998; 2000; Polletta et al., 2000) and interpreting models (e.g. Granato & Danese, 1994; Rowan-Robinson, 1995).

In this paper we report ISO observations of a complete optically selected sample of bright ($15 \leq m_B \leq 17$) quasars. The original aim of our programme was to use these data to infer any evolutionary link from "pure" AGN objects to eventual transition objects linking AGN to ULIRGs. The investigation of the complete sample would have allowed us to perform a number of statistical tests (for instance the evaluation of the bivariate luminosity function at optical-IR wavelengths) to study how the optical-infrared relation for quasars changes as a function of both luminosity and redshift. Because of the reduced sensitivity of ISOPHOT the number of observed objects is greatly reduced from the original one and the number of detection is also consequently too small to allow reliable statistics. Nevertheless, a number of different properties of the far-IR emission of optical quasars can be inferred from these data and help understanding the expected behaviour of the type-1 AGN population in surveys from future space mission – such as SIRT-F and HSO.

2. The Sample

A statistically well defined sample of bright quasars was selected from two complete optical multicolour (U,B,V,R,I) quasar surveys: the Edinburgh Bright Quasar Survey (Goldschmidt et al., 1992) and the ESO Key-Programme "A Homogeneous Bright Quasar Survey" (Cristiani et al. 1995) in a total sky area of 888 sq. deg. The optical fluxes are in the range $15 < B < 17$, partially overlapping those of the PG survey, but with a much better photometric accuracy ($\sigma_B \sim 0.1\text{mag}$). The objects finally observed with ISO are listed in Table 1, where names (column 1), J2000 coordinates (2-3), redshifts (4), **Johnson Cousins U,B,V,R,I** magnitudes (columns 5-9), and the absolute B magnitudes are reported. The apparent B-magnitude, m_B , were taken from the Homogeneous Bright QSO survey (HBQS) (Cristiani et al. 1995) whereas B_j apparent magnitudes were derived from the Digitized Sky Survey (DSS)⁵ calibrated plates (Grazian et al., 2001). K-corrections were inferred from a QSO composite spectrum (Cristiani and Vio 1990). The apparent magnitudes are corrected for Galactic absorption using the reddening maps derived from HI and Galaxy Counts by Burstein & Heiles (1982) and the luminosity distances are derived according to the adopted Cosmology ($H_0=50 \text{ km/s/Mpc}$, $\Lambda = 0$, $\Omega = 1$).

3. The Observations

3.1. The ISOPHOT Observations

The ISOPHOT data presented here result from the merging of two distinct Open Time programmes PANDREAN and PGOLDSCH.

The observed sample consists of 34 quasars of which 21 were observed at 11.5, 60 and 160 μm and 13 at 7.5, 25, 60 and 100 μm . The log of the ISOPHOT Observations is in Table 2, **coordinates used for pointing are those listed in Table 1.**

The data were reduced with the ISOPHOT Interactive Analysis Tool (PIA Version V8.2, Gabriel et al., 1998). All data were corrected for electronics nonlinearity and cosmic particle glitches. Chopped data were then averaged: all the points corresponding to one chopper position were averaged and fitted with a polynomial curve to estimate their time behaviour. If the detector shows stability, i.e. the fitted curve converges to a constant value, this latter is used as the signal related to that chopper position. In some cases, when the integration time

⁵The online Digitized Sky Surveys (<http://archive.eso.org/dss/dss>) server at the ESO/ST-ECF Archive provides access to the CD-ROM set produced by the Space Telescope Science Institute through its Guide Star Survey group.

on source was too short, for the ISOPHOT detectors to reach the stability, the signal value was inferred by extrapolating the time-dependent signal curve to an asymptotic constant value. Data are further corrected for glitches, for orbital dependent dark current and for the signal dependence on the ramp integration time.

The same reduction procedure was applied to the associated measurements of the thermal Fine Calibration Source (FCS1), which were used to estimate fluxes.

For raster maps additional softwares were used to extract the signal, kindly provided by Ilse van Bemmelen and Martin Haas and are described in van Bemmelen et al. (2000) and Haas et al. (2000).

Table 3 lists the ISOPHOT fluxes at 7, 12, 25, 60, 100 and 160 μm (columns 2-7). 30 % of the objects have fluxes larger than 3σ at 60 μm , 5 out of 7 were detected with raster maps while only 5 out of 27 with chopper mode. No objects were detected at 7 and 12 μm (only in chopping mode) and only 4 at 25 and 100 μm . At 160 μm 6 objects were detected (3 detections obtained from the 7 raster scannings). The raster scanning observing mode shows the highest sensitivity. However at 160 μm the sensitivity could be reduced in regions where the Galactic background due to cirrus emission is high. We checked detections against cirrus emission level and the results are shown in the Appendix.

Figure 1 provides a general view of all the ISOPHOT fluxes collected in the present work. The left panels show them as a function of redshift, the right panels as a function of the B-band flux. MIR is the observed wavelength range 7 - 25 μm and FIR 100- 160 μm . The lack of detections, shown in Figure 1, can be ascribed not only to the reduced sensitivity in the chopper mode but also to the nature of the FIR emission in optical quasars, showing a deficit in the short (7 and 12 μm) and long (160 μm) observed wavelengths emission, because of the characteristic high temperature of the dust grains heated by the AGN.

Although many of the values reported in Figure 1 are upper limits, it emerges an absence of dependence of the detection rate with redshift: the detections are *randomly* spread all over the redshift range. 10 detected objects have redshifts larger than the mean redshift ($\langle z \rangle = 0.72$, median redshift is 0.7) of the sample: $z > \langle z \rangle$, while the other 10 detections have $z < \langle z \rangle$. Similarly there is little correlation between the B apparent luminosity and the FIR fluxes, with only a slight trend of larger FIR fluxes for smaller B flux. The most B-luminous objects are not correspondingly FIR-luminous and there is no scaling of the FIR fluxes according to the B-band magnitude as it was assumed computing the integration time (the smaller the magnitude the shorter the integration time). The latter was computed aiming at a uniform sensitivity in terms of $\alpha_{oIR} = \log F_{\text{blue}} - \log F_{\text{IR}} \sim -2$.

Only four objects are detected in more than one IR band: 0144-39, 1404+09, 1415+00 and 1415-00. Individual notes are given in Section 4.

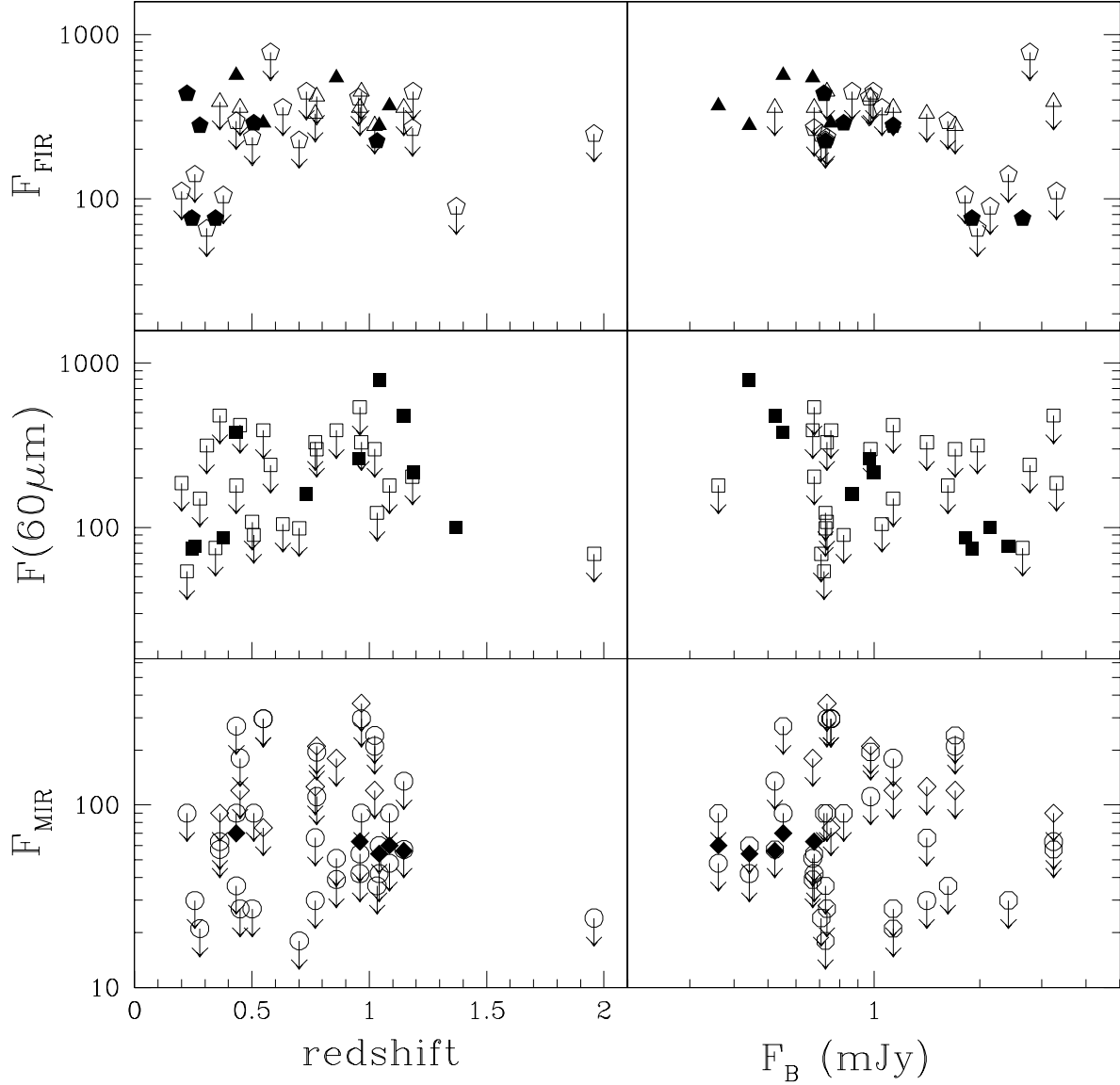


Fig. 1.— Logarithm of the ISOPHOT fluxes in mJy as a function of redshift (left panels) and of the B fluxes in mJy (right panels). The lower panels report the fluxes at 7 and 12 μm (circles) and 25 μm (diamonds), the upper panels the fluxes at 100 μm (triangles) and 160 μm (pentagons). Filled symbols correspond to detections, open to upper limits. No clear dependence is seen: upper limits and detections are equally distributed (see text). A slight trend – lower IR fluxes at large B fluxes – exists for those objects detected at 60 and 160 μm .

3.2. Additional data

3.2.1. IRAS SCANPI data

The IRAS data listed in table 3 are the result of co-added fluxes provided by IPAC SCANPI (Scan Processing and Integration Tool) program. This procedure performs a one-dimensional coaddition of all the IRAS survey data on the source. The sensitivity is comparable to that achieved by the FSC (Faint Source Catalog) for point sources (see the IPAC manual for details, <http://ipac.caltech.edu/>).

Tentative (3σ) detections among IRAS data are found for 0120-28, 0144-39, 1252+02, 1321+28, 1326-05, 1351+01, 1355+02, 1415+00, 1415-00, 2313-30, 2357-35 and are shown in boldface in table 3.

Some objects in table 3 show discrepant $60\mu\text{m}$ fluxes between the ISO and IRAS measurements. Some authors (e.g. Alton et al., 1998; Spinoglio et al., 2002) have argued that ISO fluxes are affected by a calibration error as large as 30% and found ISO fluxes in excess with respect the corresponding IRAS ones. However in some cases (1415-00 and 1415+00), even taking into account an additional 30 % error ISO values lie well above the IRAS ones. As shown in Appendix A, it is also not straightforward to attribute this discrepancy to additional cirrus emission. This contribution is expected to be larger in IRAS measurements because of the wider IRAS beams. This discrepancy may be due to variability but, at present, this issue cannot be settled and could only be addressed by regular radio observations.

3.2.2. near-IR Photometry

Counterparts within $4''$ of the QSO listed in Table 1 were detected using the 2MASS Second Incremental Data Release (<http://www.ipac.caltech.edu/2mass/>) and the corresponding J ($1.25\mu\text{m}$), H ($1.65\mu\text{m}$) and K_s ($2.17\mu\text{m}$) photometry of the 19 (out of 34) objects found is listed in table 1 (see also Barkhouse & Hall 2001). All objects with near-IR counterparts show rising near-IR spectra with magnitudes decreasing from the J to the K-band.

3.2.3. radio data

Radio data are used in this work to check whether strong non-thermal emission showing up in the radio domain would possibly affect the far-IR fluxes. The data were taken from the NVSS (NRAO VLA Sky Survey) survey (Condon et al. 1998) and from the FIRST survey (Becker *et al.* 1994) and are listed in table 1 for the 21 objects with sky positions covered by these surveys (at $\delta > -40^\circ$). **8 objects out of 21 observed in these surveys have a logarithmic ratio between the 1.4 GHz and the B-band luminosities, $\frac{L_{1.4\text{GHz}}}{L_B}$, larger than 1, i.e. are radio-loud objects.**

4. Results

4.1. Notes on individual objects

- 0051-39: has only one detection at 160 μm . The low value of the 60 μm upper limit suggests that the 160 μm flux could be eventually affected by either a galactic cirrus or radio non-thermal emission. The lack of radio data on this object does not allow us to check the latter hypothesis.
- 0059-30: has only one detection at 160 μm . This object is radio-loud and therefore this measurement could be affected by a non-thermal component but its flux is still compatible with the emission of a putative host galaxy at this wavelength.
- 0129-40: has a very clean 60 μm detection, obtained with observations in raster mode, confirming the higher sensitivity of this option.
- 0144-39: detected both at 60 and 160 μm through raster pointings. The 60 μm IRAS flux agrees with the ISO detection, while that at 100 μm is also in agreement with that at 160 μm for a thermal spectrum varying with wavelength as λ^{3-4} .
- 1252+02: detected at 160 μm and marginally at 60 μm . IRAS found fluxes at 12 and 25 μm . It is very difficult to combine these four measurements in a unique thermal component. They likely belong to different thermal components.
- 1355+02: detected at 60 μm and possibly at 100 μm by IRAS with an upper limit at 160 μm . Its spectrum can be reproduced by the emission of the circumnuclear torus.
- 1404+09: has detections at 25, 60 and 100 μm . Since it is a radio-loud these measurements could be due to the combination of two different emission mechanisms, thermal and non-thermal (see also (Polletta et al. 2000))

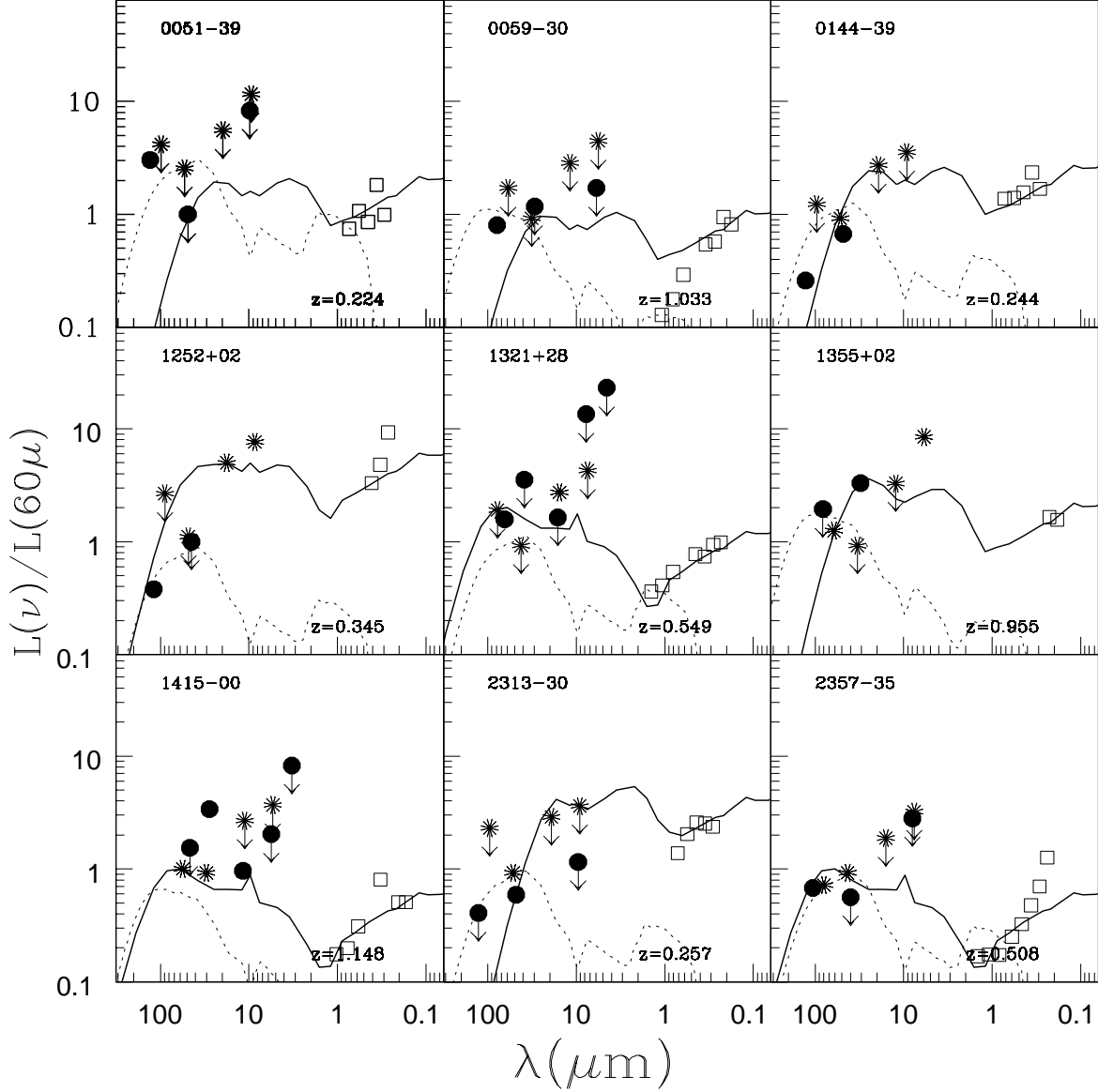


Fig. 2.— Spectral Energy Distributions (SEDs) as $\nu L(\nu)$ normalized at $60 \mu m$ of the objects reported in tables 1÷3 having at least one ISOPHOT detection. Open squares refer to optical and near-IR photometry, filled circles to ISOPHOT data, asterisks to IRAS data. The solid line corresponds to one of the models by Granato & Danese (1994) predicting the emission of dust distributed in the surrounding medium of the central AGN (see text). The dotted line is the spectrum of M82 shown here as a prototype starburst.

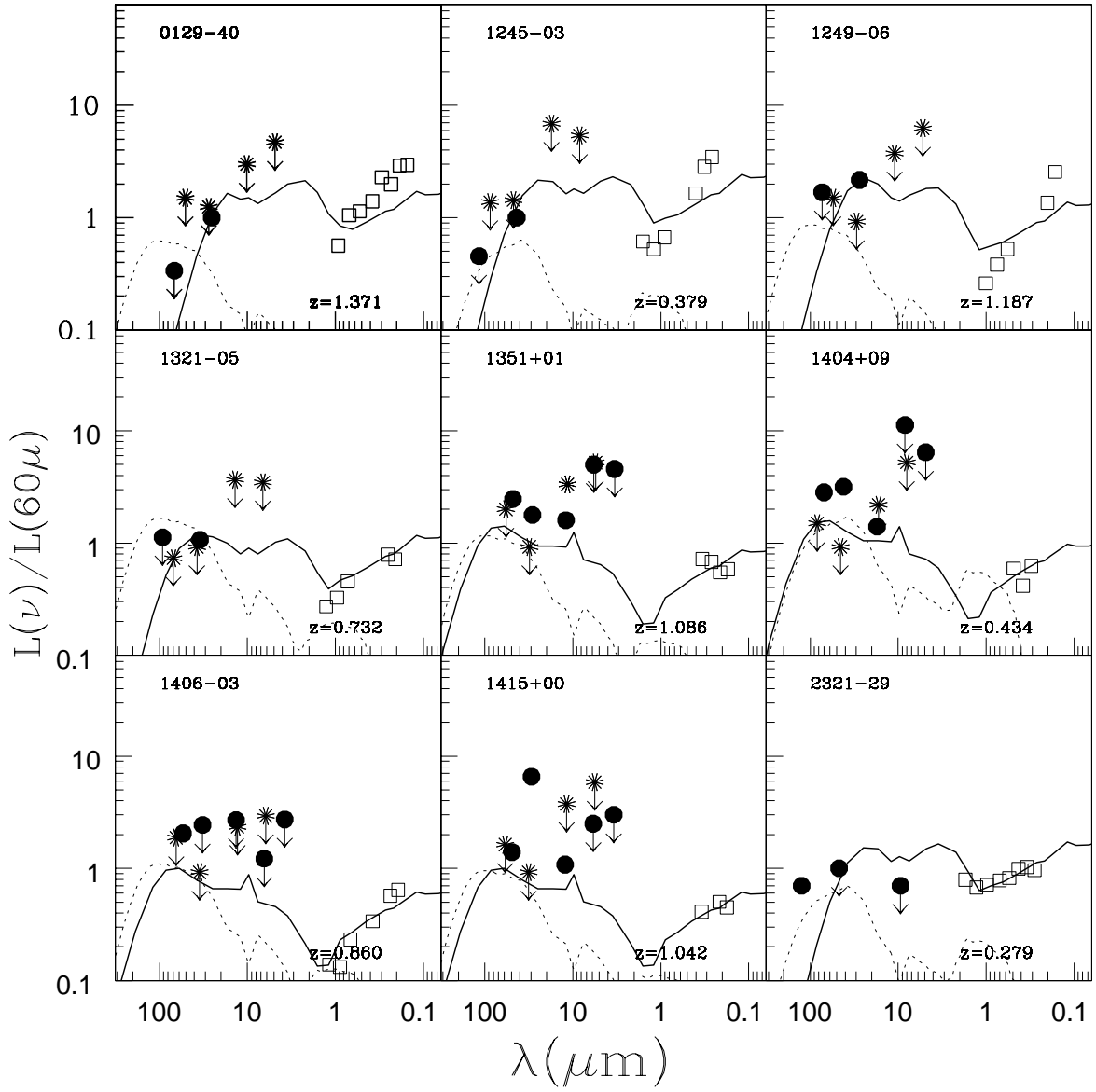


Fig. 3.— same as Figure 2

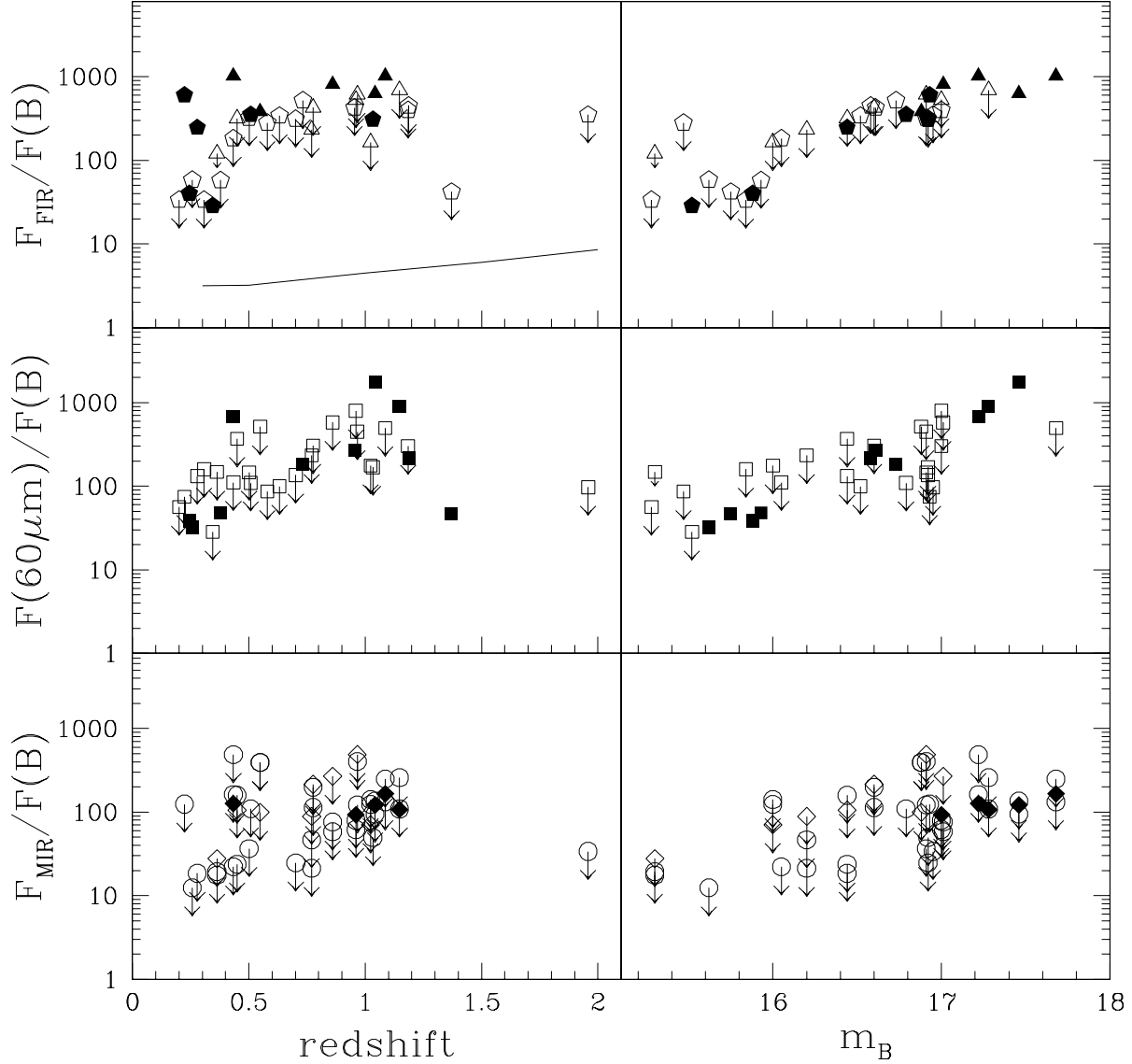


Fig. 4.— Logarithm of the ISOPHOT flux ratios versus redshift (left panels) and B apparent magnitude (right panels). The lower panels report the 7,12 and $25\ \mu\text{m}$ (MIR) fluxes, the upper panels the 100 and $160\ \mu\text{m}$ (FIR) fluxes. Symbols are as in Figure 1. A weak redshift-dependence is seen in the left panels for long wavelength fluxes, while the ratio does indeed show a dependence on m_B . In the right panels upper limits and detections are equally distributed. The solid line in the upper left panel shows the expected behaviour of the ratios $\frac{F_{\text{FIR}}}{F_B}$ in presence of extinction.

- 1406-03, 1415+00 and 1415-00 have all large fluxes at 60 and 100 μm . The latter two were detected also at 25 μm . We cannot exclude that the large 60 μm fluxes are affected by instrumental artifact. Galactic cirrus can contribute to the 100 μm emission. The 100 μm IRAS maps in these regions show a quite high background of around 80 MJy/sr with a variation from pixel to pixel around 10 %. This means that 3 ± 0.3 Jy fall on the C100 pixel. An imperfect beam switching could then mimic a source emission. However, we are not aware at present of such an effect in the ISOPHOT data.
- 2313-30: the only object observed both in raster and chopping modes but detected only with the former instrumental set-up at 60 μm . The chopper data are noisier but consistent with the raster detection.
- 2321-29 and 2357-35 have a detection only at 160 μm . Without any other FIR measurements it is tough to infer the nature of this flux. It could be ascribed to a cool component of the host galaxy as, for instance, seen in radio galaxies (van Bemmel et al., 2000).

4.2. Spectral Energy Distribution

Figures 2 and 3 show the spectral energy distribution in the object’s rest-frame of the 18 sources in the sample with FIR detections. Spectra are normalized to the 60 μm flux. Open squares correspond to the UBVRI photometry and to JHK data, filled circles to ISO measurements (down-arrows are upper limits), stars to IRAS points, which are in general upper limits but for 0105-26, 0120-28, 0144-39, 1252+02, 1351+01, 1355+02.

Although the spread in the SED appears large, mainly due to the presence of censored data, some common features can be identified: (a) all quasars with good near-IR data show a dip in the SED around $\lambda = 1 \mu m$ (b) all objects (but 0051-39) with 160 μm data show a drop of the far-IR SED beyond 100 μm .

The comparison between the optical and far-IR spectrum must take into account possible variations due to the intrinsic variability of these sources. The effect of the variability is difficult to address in detail, as it significantly depends on the time lag between the various flux measurements, the quasar absolute luminosity and increases with decreasing wavelength. From the analysis of the structure function (Cristiani et al. 1996) we should expect an average uncertainty due to variability of 0.2 magnitudes for quasars having a typical absolute magnitude $M_B \sim -26$ (0.1 for $M_B \sim -30$ and 0.3 for $M_B \sim -23$). Such variations of the flux values are still within the size of the photometric points shown in Figures 2 and 3.

The thick solid curves in Figures 2 and 3 represent the predictions of the Granato and Danese’s model (1994), which computes the expected emission of a circumnuclear torus-like dust distribution around the central nuclear source. The solution of the radiative transfer equation is required since in such tori the dust emission is self-absorbed even in the near- and mid-IR.

Dust is illuminated by the central source and reaches an equilibrium temperature which is a function of the intensity of the radiation field and of the dimensions and chemical composition of the assumed grain components. In the case shown here the chosen geometry for the dust distribution has an axial symmetry and a scaleheight along the vertical axis increasing linearly with distance (‘flared disc’). The central source is either unobscured or only partially obscured from view. This model naturally explains the SED dip around $1\ \mu\text{m}$: dust too close to the central engine attains too high temperature and sublimates.

All the curves shown in Figures 2 and 3 correspond to the same ‘face-on’ model, being all these UV-excess objects with the central source un-extincted by the surrounding torus material. The difference in the amount of IR fluxes can be accounted for by varying the dust distribution size, i.e. the dimension of the torus.

We have neither attempted to find the best-fit curves, because of the lack of sufficient constraints from the data, nor we claim that the model shown is the ‘best’ to explain these observations. Other models would be equally good (see e.g. Rowan-Robinson, 1995). However, the comparison between the predicted curves and the photometric points provides useful insights: a simple torus-like dust distribution around the central source is a too naive picture. In some cases the required dimension of the dust distribution is wide and dust could be broadly spread in a putative host galaxy disc.

To show how an additional galaxy disc emission modifies the SED, the optical-*mm* spectrum of M82, a typical local starburst, is also plotted in Figures 2 and 3, as a dotted line.

4.3. The colour plots

Figure 4 reports the colours, $\frac{F_{\text{MIR}}}{F_{\text{B}}}$, $\frac{F_{60\mu\text{m}}}{F_{\text{B}}}$, $\frac{F_{\text{FIR}}}{F_{\text{B}}}$ as a function of the B-band apparent magnitude (right panels) and of the source redshift (left panels).

The increase of the ratios with the B-magnitude can be due to several effects: (a) an observational bias, (b) cirrus emission or (c) extinction.

(a) The upper left corner of every figure panel would contain objects with large far-IR emission and bright apparent blue magnitude and therefore easily observable. Objects in the lower right corner could be missed because of a lack of sensitivity of far-IR observations. The

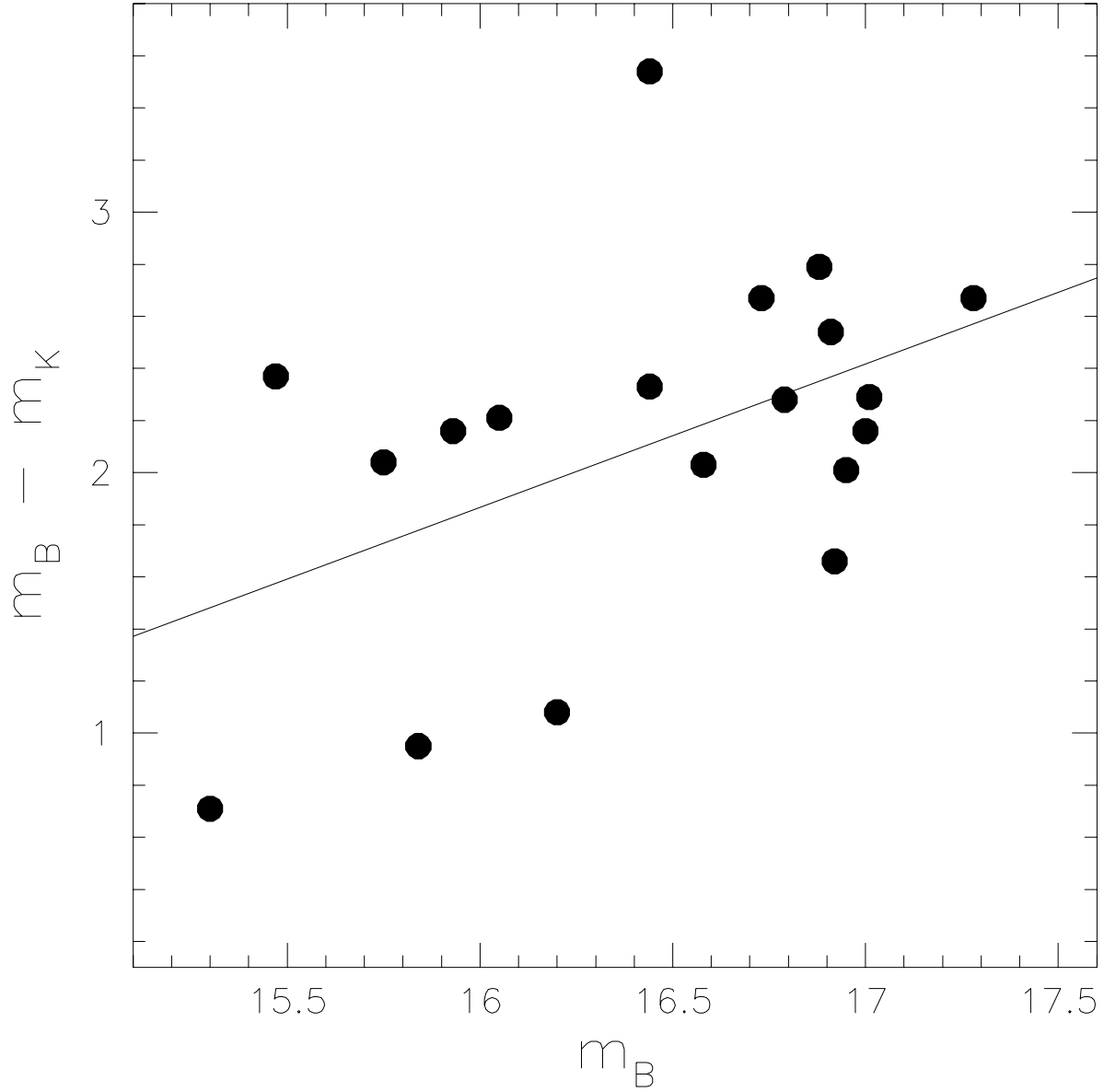


Fig. 5.— Flux ratios between the K-band and the B-band, expressed as $m_B - m_K$, against the B apparent magnitude for those objects with near-IR photometry reported in Table 1. **The solid line corresponds to the estimated linear regression line, the standard deviation, 0.575, is large and the correlation coefficient is 0.33. The hypothesis that $\frac{F_K}{F_B}$ does not vary with m_B can only be rejected at a 13% level.**

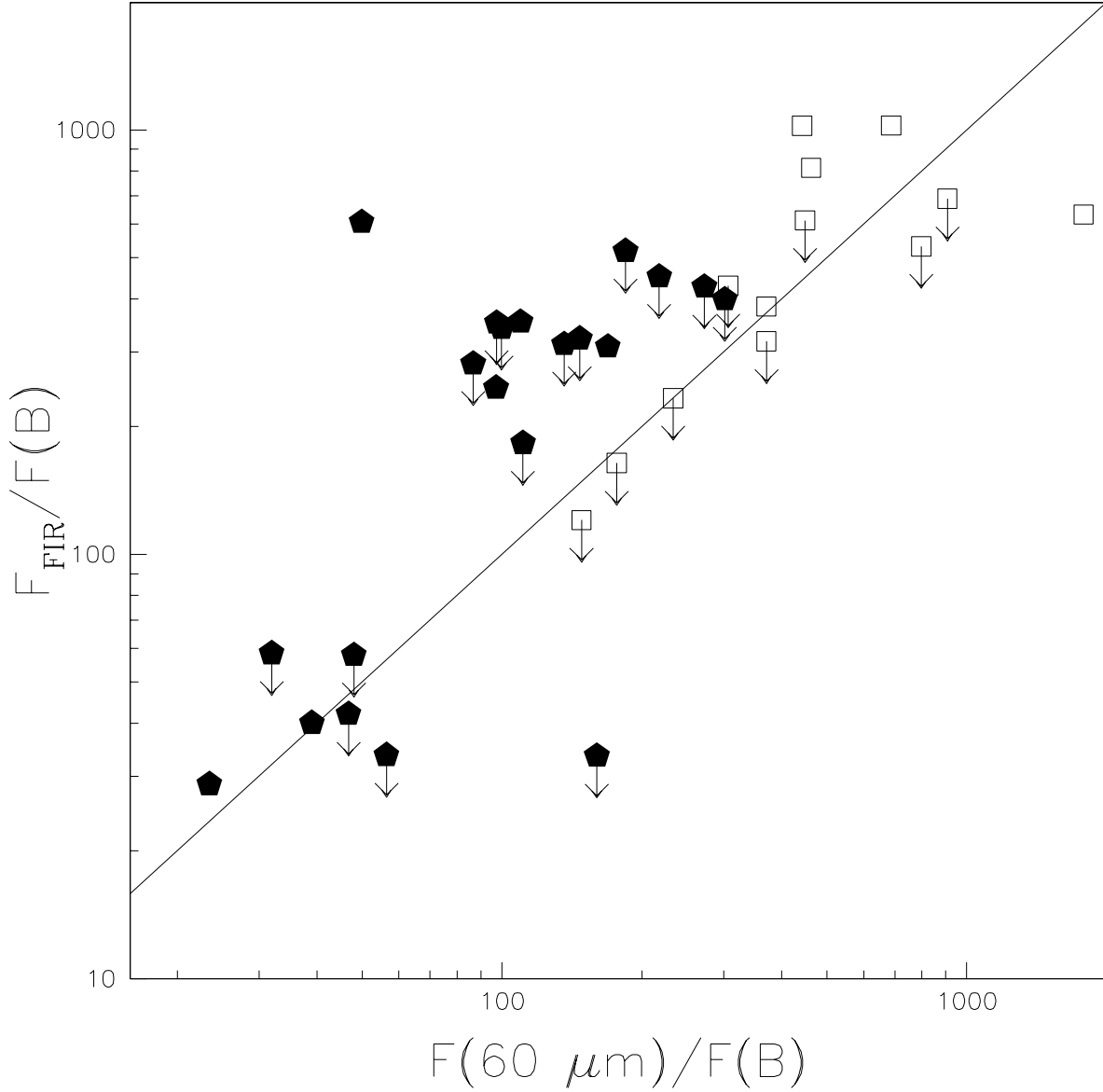


Fig. 6.— The ratio between the 100 and 160 μm fluxes and the B-band flux is shown as a function of the ratio between the 60 μm and the B flux. Open squares correspond to the 100 μm data while filled pentagons to the 160 μm ones. The straight line corresponds to a one-to-one relationship between the two colours. The outlier at $\frac{F_{160}}{F_B} \sim 600$ and $\frac{F_{60}}{F_B} \sim 50$ corresponds to 0051-39, which, as shown in Figure 2, has an extraordinarily large 160 μm flux.

upper limits distribution is quite uniform with respect to m_B , i.e. there is no accumulation of upper limits at the faint end. Sensitivity limits therefore do not seem to affect dramatically the results.

If the variation of the ratios in Figure 4 were only linked to the QSO spectrum, we would expect to see this ratio decreasing with redshift: the B-flux increases with redshift because of the negative k-correction and for a constant FIR flux $\frac{F_{\text{FIR}}}{F_B}$ would be smaller at higher redshifts ⁶. The observations show the opposite trend.

(b) The presence of Galactic cirrus emission falling in the ISOPHOT beam and affecting the far-IR fluxes has been checked using independent measurements at these wavelengths. We used the IRAS 100 μm maps in regions surrounding the observed objects (see Appendix for detail). Although in three cases the far-IR fluxes can be really enhanced because of a cirrus contribution (see Appendix) there is not a one-to-one correspondence between the ratios $\frac{F_{\text{FIR}}}{F_B}$ and the 100 μm rms values.

(c) The observed behaviour could be then ascribed to an extinction along the line of sight. The left upper panel shows a small increase of $\frac{F_{\text{FIR}}}{F_B}$ with redshift. The solid line corresponds to the expected change of this ratio when the emitted UV-optical flux ($F(\lambda) \propto \lambda^{-0.7}$) varies, because of the extinction $A(\lambda)$ and k-correction, $k(z)$, as

$$F_B = F(\lambda, z)k(z) \cdot 10^{-0.4 \cdot A(\lambda)} \quad (1)$$

We compute the ratio $\frac{F_{\text{FIR}}}{F_B}$ for blue fluxes, F_B , affected by an extinction of $A(\lambda) = E_s(B - V) * Q_{ext}(\lambda)$. We adopted as extinction law that provided by Calzetti (2001) for starburst galaxies.

Neglecting k-correction of the far-IR fluxes and correcting B-fluxes as in eq.1, more than two third of the ratios, $\frac{F_{\text{FIR}}}{F_B}$, in the upper right panel of Fig.4 would be shifted to an average value of 100. This confirms that the gross behaviour of $\frac{F_{\text{FIR}}}{F_B}$ is dictated by extinction.

Our interpretation is therefore that *fainter objects in the optical are also redder*. The redshift-dependence of IR to blue flux ratios were also investigated by Alexander et al. (2001) for a sample of ELAIS AGN with 15 μm fluxes. These authors find a ratio $\frac{f_{\text{MIR}}}{f_B}$ ranging between 2.5 and 100 independent of the source redshift. Haas et al. (2000) as well do not detect any variation of both $\frac{L_{\text{MIR}}}{L_B}$ and $\frac{L_{\text{FIR}}}{L_B}$ with redshift.

To further check the presence of dust extinction along the line of sight through the sources, we

⁶k-corrections of FIR fluxes are neglected here since, within the redshift range of our objects, the observed FIR fluxes sample the Wien region of the thermal spectrum and the resulting variation of the FIR fluxes in the restframe and observed frame is small.

plot in Figure 5 the ratio between the K-band and the B-band fluxes, expressed as $m_B - m_K$ against the B magnitude. **The straight line in Figure 5 represents to the estimated linear regression line. In spite of the large spread (standard deviation is 0.575), there is a marginal correlation (the correlation coefficient is 0.33) and a slight probability that at larger values of $m_B - m_K$ correspond larger m_B in accordance with the ratios plotted in Figure 4. However, the hypothesis that $\frac{F_K}{F_B}$ does not vary with m_B can only be rejected at a 13% level.**

4.3.1. Colour-colour plot

In Figure 6, 100 and 160 μm fluxes, normalized to the B-band flux, $\frac{F_{FIR}}{F_B}$, are shown against the 60 μm flux, $\frac{F_{60}}{F_B}$. The two colours are tightly related: an increase of the long wavelength flux with respect to the B-band flux corresponds to an equivalent enhancement of the 60 μm flux with respect to the optical one. The two far-IR fluxes are therefore related and very likely belong to the same thermal component. As a comparison a straight line showing a one-to-one relationship is drawn in Figure 6. The ratio $\frac{F(60\mu m)}{F_{FIR}}$ can be then used as an estimation of the dust colour temperature for that thermal component.

4.4. Dust Temperature

Customarily the spectral indices, α , for a $f_\nu \propto \nu^\alpha$ SED are defined as

$$\alpha(\nu_1, \nu_2) = \log \frac{f(\nu_1)}{f(\nu_2)} - \log \frac{\nu_1}{\nu_2} \quad (2)$$

and simply related to colours. Figure 7 reports $\alpha(60\mu m, MIR)$ versus $\alpha(FIR, 60\mu m)$. According to our previous finding (§4.3) this latter is inversely proportional to the *warm* dust temperature, T_{wd} . Although many points in the diagram are upper/lower limits there seems to be a trend: the relative emission at shorter wavelengths (7, 12 and 25 μm) with respect to the 60 μ emission decreases as T_{wd} increases. This colour-colour diagram was widely used in the past as a tool to detect and discriminate between different types of activity in the nuclear and circumnuclear regions of galaxies (see e.g., Canalizo & Stockton (2001) and references therein). Different kinds of objects (QSOs/Seyferts, starbursts and ULIRGS) occupy distinct loci in such a diagram: objects for which FIR fluxes are dominated by dust reradiation are located in the lower right corner (in our convention at lower T_{wd} and lower $\alpha(60\mu m, MIR)$), while objects with strong non-thermal emission, such as optically selected QSOs, are in the upper left corner. Indeed PG quasars observed by IRAS are preferentially

found at $-2 < \alpha(60\mu m, \text{MIR}) < 1$ and $-2 < \alpha(\text{FIR}, 60\mu m) < 0$ partially overlapping the region of the diagram where *transition* objects are found (Canalizo & Stockton, 2001). To show that in detail we plot in Figure 7 the location of the QSOs observed by IRAS at redshift lower than 2 and studied by Andreani, Franceschini & Granato et al. (1999).

In Figure 8 the ratio $\frac{F(60\mu m)}{F_{\text{FIR}}}$ is plotted against the absolute B magnitude. With all the limits of this analysis due to the poor information on the FIR fluxes, it appears that no statistically significant correlation is present between the B luminosity and the warm dust colour temperature, T_{wd} .

If M_{B} is linked to the nuclear emission, while $\frac{F(60\mu m)}{F_{\text{FIR}}}$ is only a dust property, it seems that no strong relation exists between the energy emitted by the nuclear source and that emitted in the FIR. Similar findings were already reported by Andreani, Franceschini & Granato (1999) for an inhomogeneous sample of optical quasars with IRAS and mm-wavelengths fluxes. For their sample no relation was found between the dust mass and the absolute B-magnitude M_{B} . McMahon et al. (1999) and Omont et al. (2001) do not detect any dependence of the sub-mm fluxes on the optical luminosity in high redshift quasars. All these results could be fitted into a picture in which the emission from the nuclear source is not tightly related to the physics (the dust properties: temperature, mass and luminosity) of the surrounding medium and argues in favour of the hypothesis that most of the FIR luminosity is linked to a concurrent starburst and trace activity in the host galaxy (see also Clements, 2000). This result is also related to dynamical studies aiming at the search for BHs in galaxy centres. These investigations show that although there is a strong one-to-one correspondence between the central BH mass and bulge luminosity no detectable correlation is found between the BH mass and the luminosity of galaxy discs (see e.g. Kormendy & Gebhardt, 2001).

4.5. Luminosity plots

Figure 9 shows the ratio between the far-IR, L_{FIR} , and the B-band, L_{B} , luminosities versus the bolometric luminosity, L_{bol} . On the y-axis we plot $\frac{\sum_i \nu_i f(\nu_i)}{\nu_{\text{B}} f(\nu_{\text{B}})}$ i.e. the ratio between the far-IR luminosity L_{FIR} , as the sum of the different far-IR data, and the blue-band luminosity computed from the absolute B magnitude: $10^{-0.4 M_{\text{B}} + 28.523}$. On the x-axis the bolometric luminosity is shown:

$$L_{\text{bol}} = 4\pi d_L^2 \int d\nu f(\nu) \quad (3)$$

where d_L is the luminosity distance. L_{bol} is computed from UV to FIR. Down-arrows correspond to objects undetected in all bands, triangles to those with one detection, filled circles

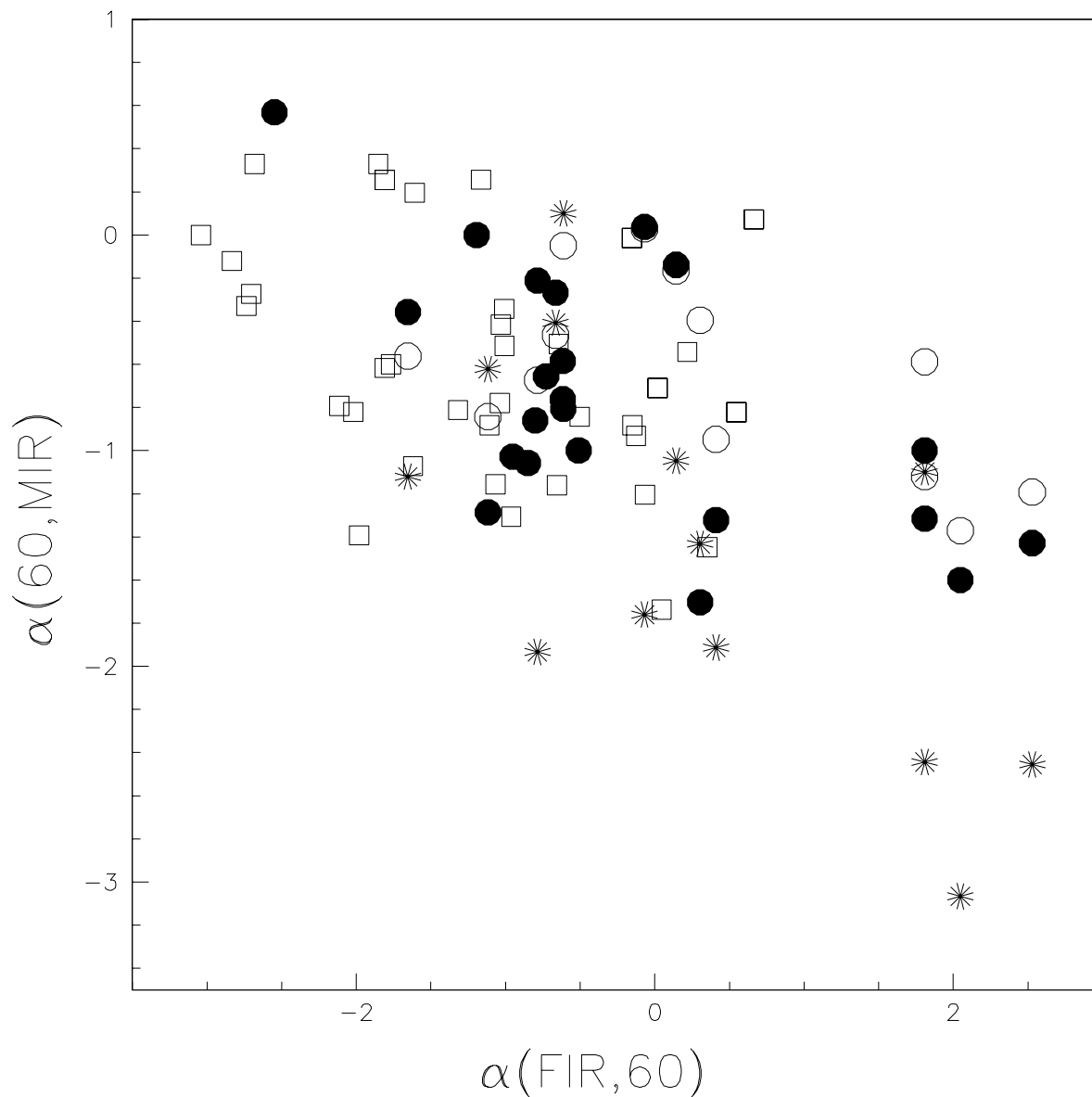


Fig. 7.— The ratio between $60\mu\text{m}$ flux and MIR fluxes is shown as a function of the ratio between FIR and $60\mu\text{m}$ fluxes. Ratios are defined by equation 4.4. Asterisks correspond to the $25\mu\text{m}$ data, filled circles to $12\mu\text{m}$, open circles to $7\mu\text{m}$ ones. Open squares correspond to QSOs at $z \leq 2$ reported in Andreani, Franceschini & Granato (1999). Distinct areas can be identified from AGN dominated (in the upper left corner) to Starburst dominated objects (in the lower right corner), according to the expected dominant emitting mechanism in the object SED from non-thermal to thermal.

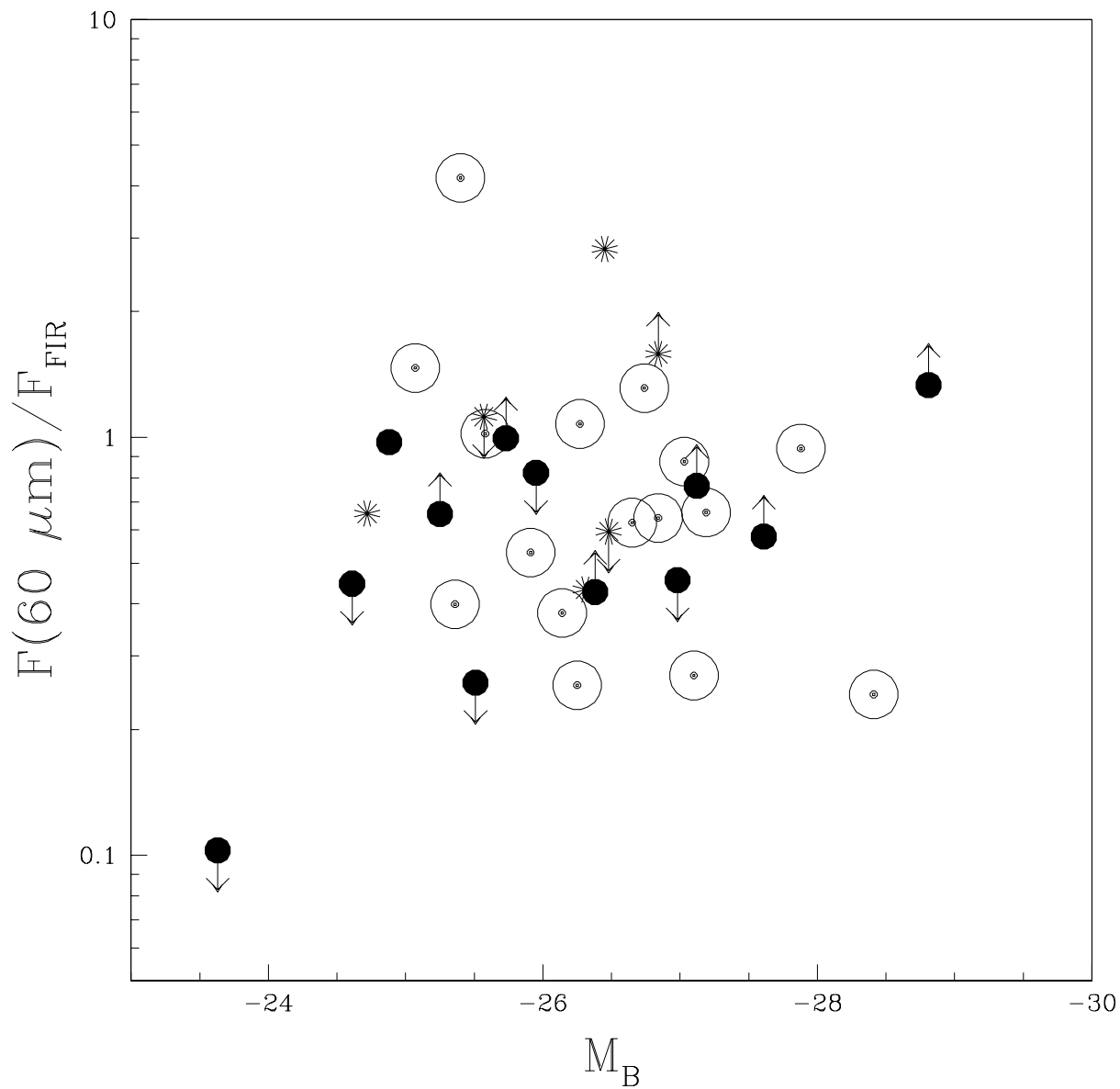


Fig. 8.— The ratio $\frac{F(60\mu\text{m})}{F_{\text{FIR}}}$, which is proportional to the dust temperature, T_{wd} , as a function of the absolute B magnitude, M_B . Asterisks refer to the 100 μm data, filled circles to the 160 μm data, \odot symbols to ratios with upper limits on both fluxes.

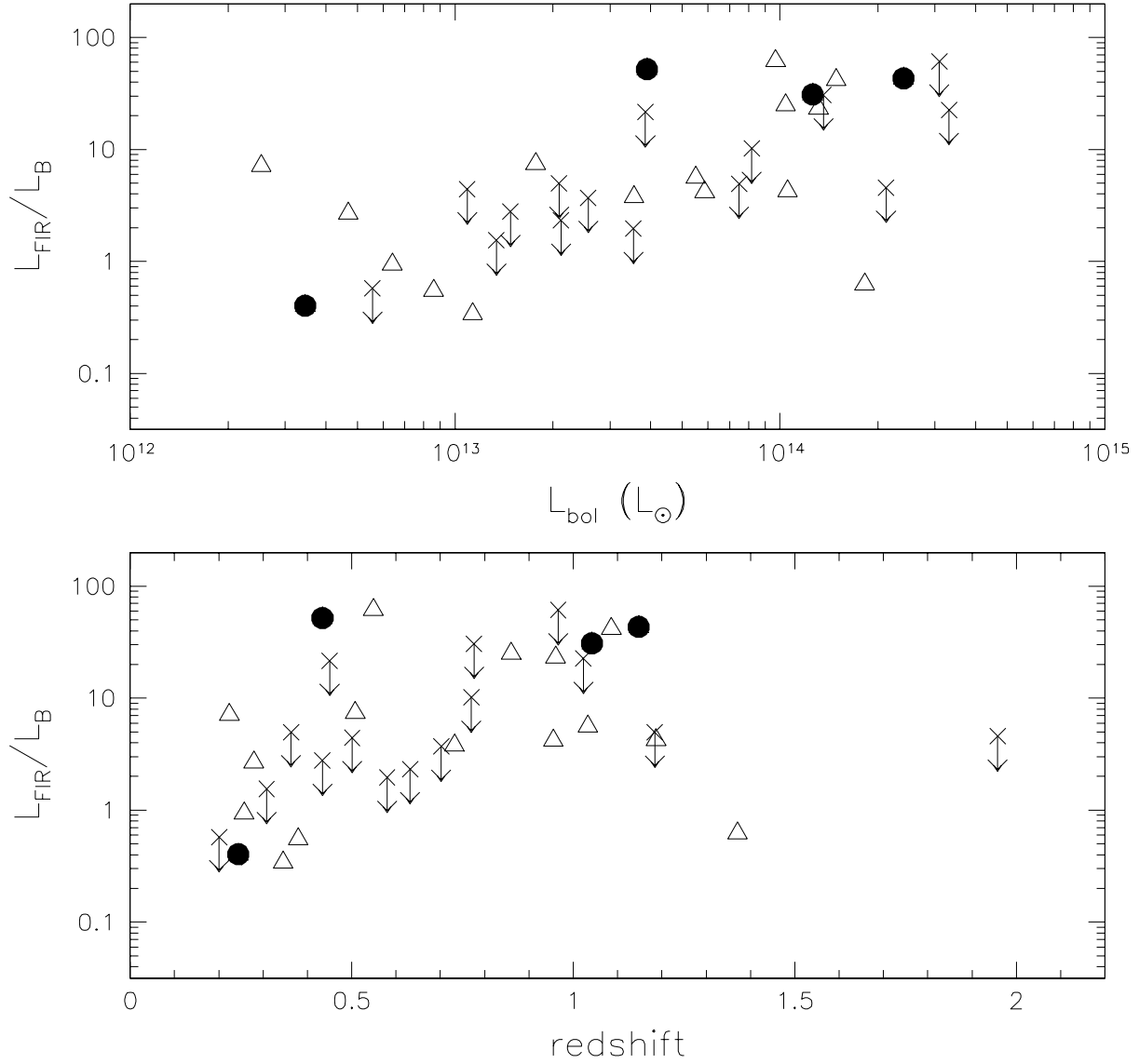


Fig. 9.— The ratio between the far-IR, L_{FIR} , and the B-band, L_{B} , luminosities against the bolometric luminosity, L_{bol} (upper panel) and against the source redshift (lower panel) is shown. Triangles correspond to those objects with only one ISOPHOT detection, filled circles to those with two or three detections, downarrows to undetected objects.

to those detected at least in two bands. L_{FIR} could well be underestimated for those objects with only one or two detected fluxes. Sampling the Wien region of a thermal spectrum with a characteristic temperature of 40-100 K at only one or two frequencies means to underestimate the total luminosity of a factor between 2 and 5 with respect to the integral over the whole frequency range.

Only five objects have clearly a $\frac{L_{\text{FIR}}}{L_{\text{B}}}$ ratio lower than 1, 14 detected ones have $\frac{L_{\text{FIR}}}{L_{\text{B}}} > 1$ of which 7 have FIR luminosity more than one order of magnitude higher than the blue one. There is a clear trend of increasing $\frac{L_{\text{FIR}}}{L_{\text{B}}}$ with increasing bolometric luminosity. This means that the FIR luminosity becomes increasingly important as the bolometric luminosity increases. A similar behaviour is seen in nearby ultraluminous IR Galaxies (ULIRGs) (Sanders and Mirabel, 1996) and has been associated to the increased central concentration of molecular gas. Because of the high extinction the relative role of nuclear starburst and AGN activity is hard to disentangle in ULIRGs but there seems to be an enhancement of AGN contribution to the overall energy budget as the bolometric luminosity increases. Furthermore, in the Unified Scheme of AGN an enhancement of the $\frac{L_{\text{FIR}}}{L_{\text{B}}}$ ratio is expected, since the reprocessed emission by the dusty torus emerges isotropically in the FIR. The colour axis $\frac{L_{\text{FIR}}}{L_{\text{B}}}$ should be related to the viewing angle to the torus with more inclined objects having larger $\frac{L_{\text{FIR}}}{L_{\text{B}}}$ therefore lying on the right-hand side of the diagram.

The lower panel in Figure 9 shows the behaviour of the ratio $\frac{L_{\text{FIR}}}{L_{\text{B}}}$ against the source redshift: with the present data it is not possible to detect any evolution of the ratio $\frac{L_{\text{FIR}}}{L_{\text{B}}}$ with redshift.

5. The quasar composite spectrum

The objects presented in this work are randomly drawn from a complete sample of optically selected quasars (see §2) and can be considered representative of the entire quasar population. If we assume that the radio-quiet quasars can be modeled as a homogeneous population, a spectrum can be built via observations at fixed frequencies of targets at different redshifts. This analysis exploits the whole spectral information from the optical to the FIR and helps outlining possible general features of the emitting mechanisms and the physics of the QSO environment. The spectrum is built by dividing the available wavelength range in bins. In each bin an average of the fluxes at that wavelength is computed. The errorbars shown are those related to the averages. Uncertainties on the flux scale lie well within the large errorbars.

Figure 10 shows the average spectrum in the QSO restframe. The spectrum is nor-

malized at $\lambda_B = 0.44 \mu\text{m}$. Averages are computed in each wavelength bin with the survival statistics which take into account the censored data (Feigelson 1990). Detections with a suspected contribution from IR-cirrus were included as upper limits. A well defined IR component peaking at 10-30 μm and dropping steeply above 100 μm is evident. The spectral shape of the far-IR component is characteristic of a thermal origin. It can be speculated whether it is due to starburst emission in the host galaxy and/or to a dusty torus around the central source. In order to derive constraints to the available parameters on the dust distribution, we can compare the data with available models. Figure 10 reports three different spectral energy distributions predicted by the Granato & Danese 's model (1994) (see §4.2). We restrict ourselves to models which allow UV-optical photons to escape from the nuclear source since the quasars were selected on the basis of their UV-excess. The dust distribution around the central source should be compact because of the sharp cut-off at long wavelengths of the FIR bump. A larger bump would imply larger temperature distribution and very likely larger spatial dimension of the dust distribution.

The solid line corresponds to face-on (with a 'naked' nuclear source) compact (i.e. the ratio between the inner and outer radius of the torus $\frac{r_{in}}{r_{out}}=800$) configuration of the torus and an optical depth τ at 0.3 μm of 30; the dotted line to a 45° inclined torus with larger dimension ($\frac{r_{in}}{r_{out}}=1000$) and same τ , the dashed line to a 45° inclined torus ($\frac{r_{in}}{r_{out}}=1500$) with higher absorption, $\tau=60$. The curve in better agreement with the available photometric points is that corresponding to the larger optical depth (dashed line) and therefore the strongest dust self-absorption around 10-30 μm .

6. Conclusions

A sample of optically selected quasars was observed with ISOPHOT between 7 and 160 μm , with the following results:

- The sample shows homogeneity in mid and far-IR properties: the mid and far-IR colours depend neither on the redshift nor on the absolute B-magnitude and there is no correlation between the blue magnitude and the ISOPHOT fluxes.
- The detection rate is not a function of redshift (10 detected objects have $z < 0.7$, the other 10 have $z > 0.7$, where 0.7 is the median redshift of the redshift distribution) consistently with the negative K-correction implied by a thermal spectrum.
- The long wavelengths ($\lambda=60,100$ and 160 μm) fluxes are tightly related and likely arise from the same thermal component.

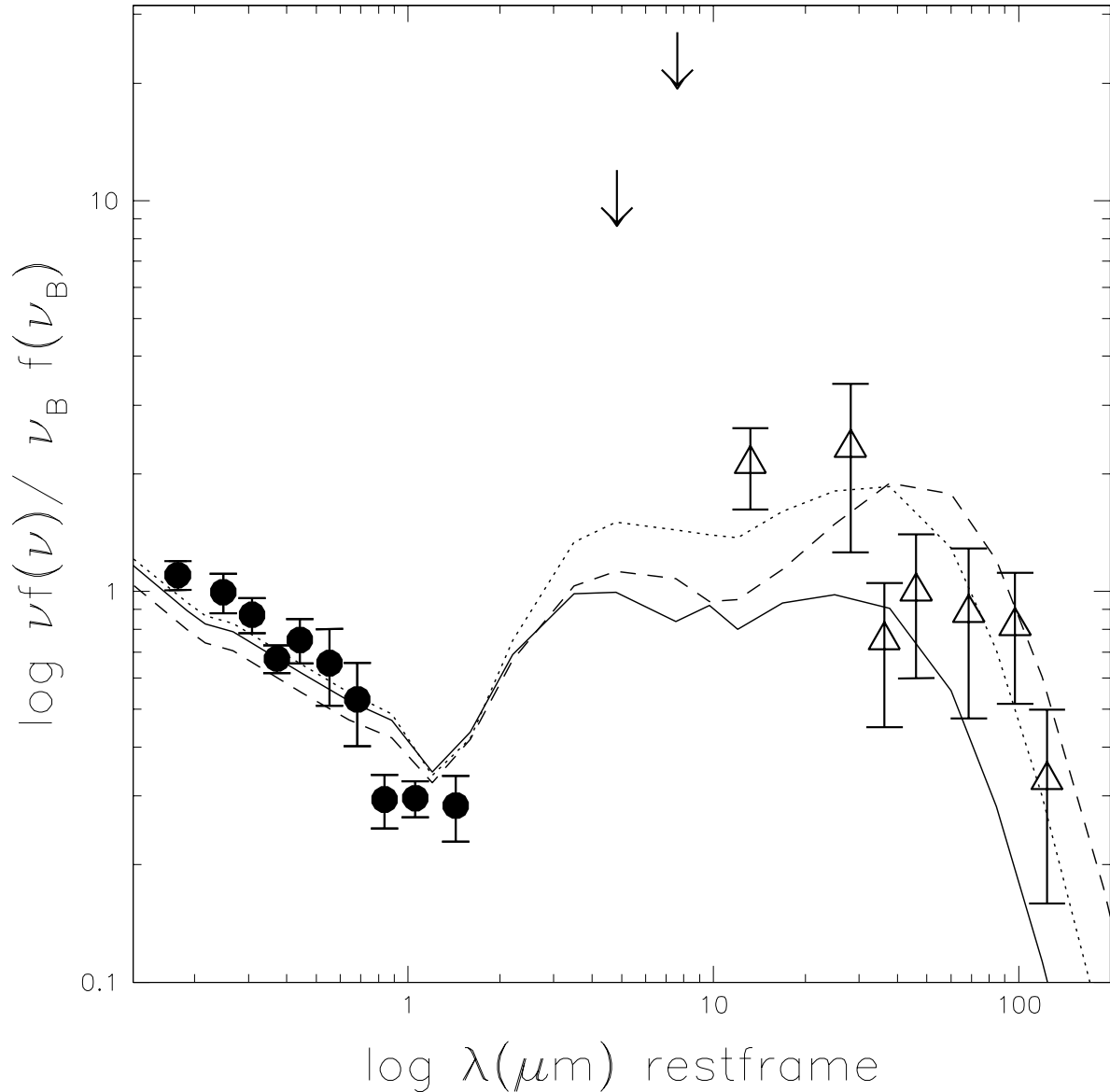


Fig. 10.— The average spectrum in the QSO restframe. The spectrum is normalized at $\lambda_B = 0.44 \mu\text{m}$. Filled circles correspond to the optical and near-IR data, open triangles to the ISOPHOT measurements discussed in this paper. The lines going through the data show the predictions of the models by Granato and Danese (1994) which are able to fit the QSO SED (see §4.2). The solid line corresponds to a face-on compact configuration of the torus and absorption at $30 \mu\text{m}$ of $\tau=30$, dotted line to a 45° inclined torus with larger dimension and same τ , the dashed line to a 45° inclined torus with higher absorption, $\tau=60$.

- Objects with fainter blue magnitudes, m_B , have larger ratios between the FIR ($\lambda > 60\mu m$) fluxes and the blue band flux, $\frac{f_{FIR}}{f_B}$. We ascribe this behaviour to a larger extinction along the path to the central source.
- The colour-colour diagram $\alpha(60\mu m, MIR)$ versus $\alpha(FIR, 60\mu m)$ shows that the objects of the present sample span a wide range of properties from AGN-dominated ones (low $\alpha(FIR, 60\mu m)$, i.e. large dust temperature) to starburst-dominated ones (low $\frac{60\mu m}{MIR}$ and large $\frac{FIR}{60\mu m}$).
- No statistically significant correlation is detected between the absolute B-magnitude, M_B and the warm dust temperature, T_{wd} . If M_B mainly reflects the nuclear emission and the FIR fluxes the emission of the surrounding dust, it seems that no relation exists between the energy emitted by the nuclear source and that by dust. The latter could rather be a tracer of the starburst activity in the host galaxy.
- Even in an optically selected sample the amount of energy emitted in the far-IR, L_{FIR} , is on average a few times larger than that emitted in the blue, L_B . The ratio $\frac{L_{FIR}}{L_B}$ does not show any clear variation with redshift but increases with the bolometric luminosity, L_{bol} . This behaviour is similar to that seen in local ULIRGs, possibly because of an increased central concentration of molecular gas. In the Unified Scheme of AGN an enhancement of the $\frac{L_{FIR}}{L_B}$ ratio is expected in the more inclined objects for which the viewing angle goes through the torus, i.e. through a more extincted line of sight.
- The QSO Composite Spectrum, i.e. the average spectrum built in the QSO restframe, shows a broad far-IR bump at 10-30 μm which could be due either to a starburst emission in the host galaxy or to a dusty torus around the central source as predicted in the unified scheme of AGN.

Restricting our analysis to only the QSO SED one could argue that the best picture fitting the data is that of a circumnuclear dusty torus. However other arguments presented also in this paper (the colour-colour diagram, the lack of relation between the power of the nuclear source and the dust temperature and the increase in the ratio $\frac{L_{FIR}}{L_B}$, see Figures 7, 8, 9) suggest that a contribution from a starburst from the host galaxy is quite unavoidable.

This publication makes use of data products from the Two Micron All Sky Survey, which is a joint project of the University of Massachusetts and the Infrared Processing and Analysis Center/California Institute of Technology, funded by the National Aeronautics and Space Administration and the National Science Foundation.

Based on photographic data obtained using The UK Schmidt Telescope. The UK Schmidt Telescope was operated by the Royal Observatory Edinburgh, with funding from the UK Science and Engineering Research Council, until 1988 June, and thereafter by the Anglo-Australian Observatory. Original plate material is copyright the Royal Observatory Edinburgh and the Anglo-Australian Observatory. The plates were processed into the present compressed digital form with their permission. The Digitized Sky Survey was produced at the Space Telescope Science Institute under US Government grant NAG W-2166.

One of the authors (PA) warmly thanks Ilse van Bemmelen for her help during the data analysis and for her permission of using her software. PA acknowledges the fundamental help of the ISOPHOT Data Center in Heidelberg in the data reduction and MPE for hospitality. Alexander von Humboldt Foundation for support is acknowledged. Part of this work was funded by the Italian Space Agency (ASI) under contract ARS-98-226, ASI-I-R-105-2000.

A. Appendix: Detections against cirrus level

Figure 11 reports the detected fluxes and upper limits at 100 and 160 μm against the r.m.s. values of the cirrus emission as estimated from the 100 μm IRAS maps in the sky positions corresponding to the source location. Upper limits are shown by downarrows. No correlation between the two quantities is apparent, with the possible exception of the three sources 0051-39, 1404+09, 1406-03. For these three cases the large observed flux could be affected by cirrus emission as discussed in section 4.1. However, 0051-39, 1404+09 are radio-loud objects and the tail of the radio emission could also contribute to the FIR fluxes.

REFERENCES

- Alexander D.M. La Franca F., Fiore F., Barcons X., Ciliegi P., Danese L., Della Ceca R. et al., 2001 ApJ 554, 18
- Andreani P., Franceschini A., Granato G.L., 1999 MNRAS 306, 161
- Barkhouse W.A., Hall P.B., 2001 AJ 121, 2843; Erratum AJ 122, 496
- Becker, R. H., White, R. L., & Helfand, D. J. 1994, Astronomical Data Analysis Software and Systems III, ASP Conference Series, v. 61, eds. D. R. Crabtree, R. J. Hanisch, & J. Barnes, p. 165
- Boyle B.J. et al., 2001, MNRAS 317, 1014

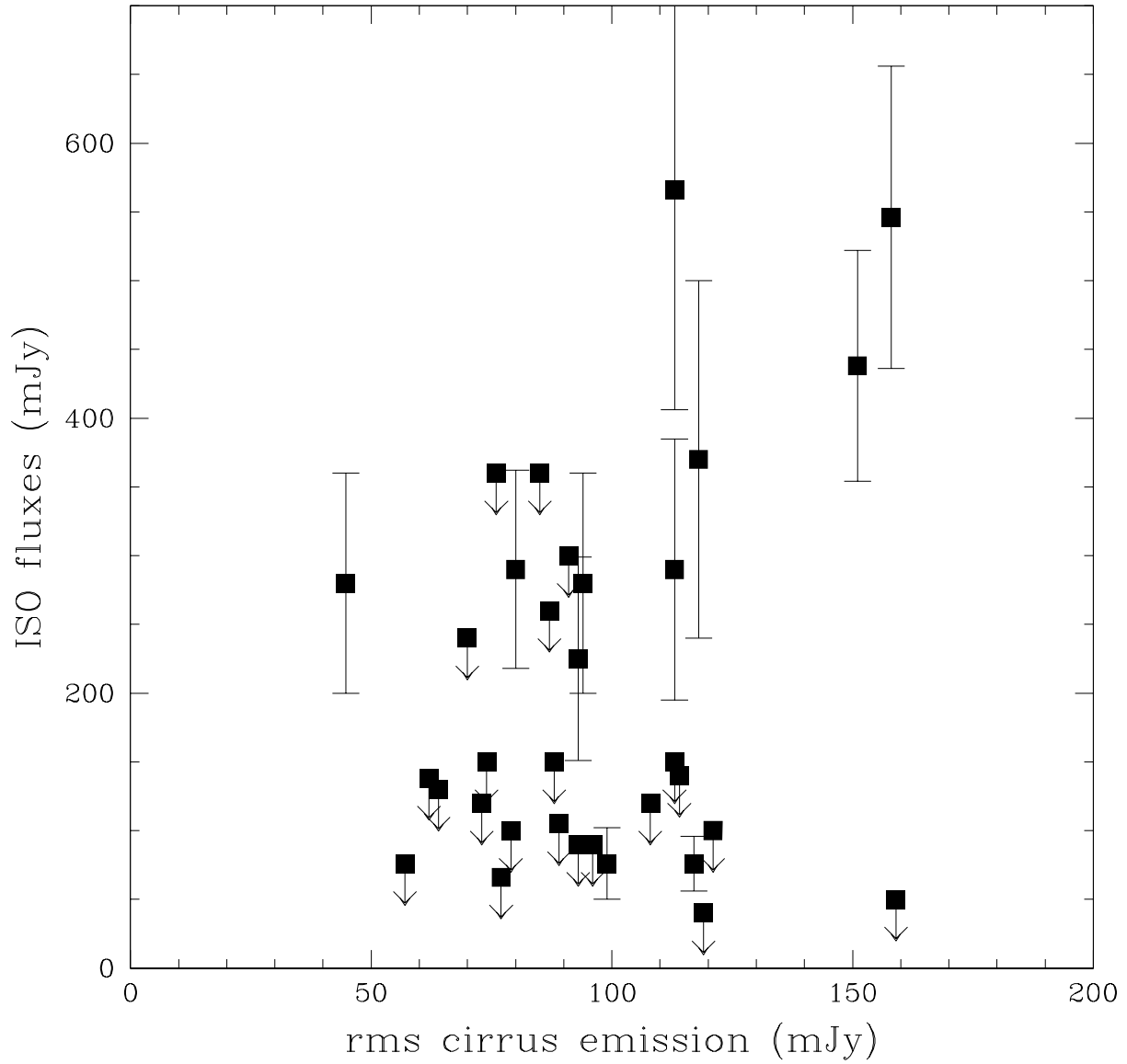


Fig. 11.— The 100 and 160 μm fluxes against the rms values of the Galactic cirrus emission at 100 μm as estimated from the IRAS maps towards the sources observed by ISO. Upper limits are indicated as downarrows. The three higher values of the ISO fluxes correspond to 0051-30, 1404+09 and 1406-03, the first two are also radio-loud objects.

- Burstein D. & Heiles C., 1982 AJ 87, 1165
- Calzetti D., 2001 in *FIRSED2000 Workshop on The Far-Infrared and Submillimeter Spectral Energy Distributions of Active and Starburst Galaxies*, eds P. Barthel, B. Wilkes and I. van Bemmel, New Astronomy Reviews 45, 601 (Elsevier, The Netherlands).
- Canalizo G., Stockton A., 2001 ApJ 555, 719
- Carilli C.L., Bertoldi F., Menten K.M., Rupen M.P., Kreysa E., Fan X., Strauss M.A., Schneider D.P., Bertarini A., Yun M.S., Zylka R., 2000, ApJ 533, L13
- Chini R., Biermann P.L., Kreysa E., Gemünd H.P., 1989b, A&A, 221, L3-L6
- Clements D.L., 2000, MNRAS 311, 833
- Condon J.J., Cotton W.D., Greisen E.W., Yin Q.F., Perley R.A., Taylor G.B. & Broderick J.J. 1998, AJ, 115, 1693.
- Cristiani S. & Vio R., 1990 A&A 227, 385
- Cristiani S. et al., 1995 A&A Sup. 112, 347
- Cristiani S., Trentini S., La Franca F., Aretxaga I., Andreani P., Vio R., Gemmo A., 1996, A&A, 306, 395
- Gabriel C., Acosta-Pulido J., Heinrichsen I., 1998, Proc. ADASS VII, ASP Conf. Se. 145, eds R. Albrecht, R.N. Hook H.A. Bushouse (San Francisco)
- Feigelson, E. D. “Censored Data in Astronomy”, *Errors, Bias and Uncertainties in Astronomy*, eds. C. Jaschek and F. Murtagh, (Cambridge U. Press: Cambridge) p. 213, 1990.
- Granato G.L., Danese L., 1994 MNRAS 268, 235
- Grazian A., Cristiani S., D’Odorico V., Omizzolo A. Pizzella A., 2000 AJ 119, 2540
- Goldschmidt P. et al., 1992 MNRAS, 256, 65p
- Haas M., Chini R., Meisenheimer K., et al. 1998, A&A 338, L33
- Haas M., Müller S.A.H., Chini R., Meisenheimer K., et al. 2000, A&A 354, 453
- Kormendy J. & Gebhardt K., 2001, in *The 20th Texas Symposium on Relativistic Astrophysics*, ed. H. Martel & J.C. Wheeler, AIP Conference Proceedings 586.

- McMahon R.G. et al., 1999, MNRAS 309, L1
- Oyabu S., Kawara K., Tsuzuki Y., et al., 2001, A&A 365, 409
- Omont A., McMahon R.G., Cox P., Kreysa E., Bergeron J., Pajot F., Storrie-Lombardi L.J., 1996b, A&A 315, 1
- Omont A., McMahon R.G., Cox P., Kreysa E., Storrie-Lombardi L.J., 2001, A&A,
- Polletta M., Courvoisier T.J.-L., Hooper E.J., Wilkes B.J., 2000, A&A 362, 75
- Rowan-Robinson, M., 1995 MNRAS 272, 737
- Sanders D.B., Phinney E.S., Neugebauer G., Soifer B.T., Matthews K., 1989, ApJ 347, 29-51
- Sanders D.B., Mirabel F.I. 1996, AR&A 34, 725
- van Bemmell I., Barthel P., de Graauw T., 2000, A&A 359, 523
- Veron-Cetty M., Veron P., 1998 (8th Edition), ESO Sci. Rep. 18 (1)

Table 1. Optical and near-IR Photometry of Quasars

Name	R.A.(J2000)	dec(J2000)	z	m _B	m _U	m _V	m _R	m _I	m _J	m _H	m _K	M _B	F
0034-70	0 34 05.0	-70 25 54	0.363	15.30	...	15.50	17.70	...	16.10	15.61	14.59	-26.27	
0049-29	0 51 38.1	-29 23 13	0.308	15.84	16.66	14.81	13.96	13.59	14.99	14.37	14.89	-25.40	
0051-39	0 54 09.5	-39 16 52	0.224	16.93	16.92	17.30	16.62	16.51	-23.63	
0059-30	1 02 00.7	-30 18 28	1.033	16.92	16.41	17.01	16.64	...	16.11	15.77	15.26	-26.98	
0105-26	1 05 58.9	-26 06 22	0.776	16.60	...	16.90	15.60	-26.65	
0120-28	1 22 36.6	-28 43 20	0.434	16.05	15.48	15.71	15.84	15.91	15.48	14.68	13.84	-25.91	
0129-40	1 31 43.9	-40 36 54	1.371	15.75	15.06	15.72	15.13	15.16	14.68	13.89	13.71	-28.81	
0144-39	1 46 12.4	-39 23 06	0.244	15.88	15.57	15.87	15.56	15.07	-24.88	
0203-08	2 03 22.5	-8 43 37	0.770	16.20	16.50	16.90	...	15.84	15.48	15.12	-27.03	<24.5	
1245-03	12 47 35.0	-3 50 09	0.379	15.93	15.04	16.07	15.41	14.80	13.77	-25.73	<
1249-02	12 51 51.4	-2 23 36	1.184	17.00	16.45	17.10	15.80	15.30	14.84	-27.19	
1249-06	12 51 56.4	-7 05 02	1.187	16.58	15.22	15.52	14.99	14.55	-27.61	
1252+02	12 55 19.6	1 44 13	0.345	15.52	14.13	15.48	-25.95	
1321-05	13 24 14.8	-6 04 38	0.732	16.73	16.16	15.24	14.72	14.06	-26.38	
1321+28	13 21 15.9	28 47 19	0.549	16.88	16.15	16.69	16.20	...	15.39	14.81	14.09	-25.57	<
1323+29	13 23 20.9	29 10 07	0.966	16.91	16.17	16.83	16.70	-26.84	<
1326-05	13 29 28.6	-5 31 36	0.580	15.47	15.02	15.59	14.51	13.91	13.10	-27.10	
1351+01	13 51 28.4	1 03 39	1.086	17.68	16.94	17.00	16.50	-26.31	<
1355+02	13 58 24.0	2 13 44	0.955	16.61	16.00	-27.12	<
1404+09	14 04 11.1	9 37 38	0.434	17.22	...	17.22	16.40	-24.72	
1406-03	14 06 10.8	-3 19 13	0.860	17.01	16.21	...	16.70	...	15.90	15.63	14.72	-26.48	<
1415+00	14 15 49.7	0 53 56	1.042	17.46	16.91	...	16.80	-26.45	<
1415-00	14 15 28.8	-0 26 34	1.148	17.28	16.61	...	15.90	...	15.73	15.33	14.61	-26.84	<
1424-00	14 26 58.5	-0 20 57	0.632	16.52	15.99	-26.25	<
1528+28	15 28 40.6	28 25 30	0.450	16.44	15.79	16.39	16.60	...	15.42	14.67	14.11	-25.58	
1630+37	16 30 18.7	37 19 03	0.960	17.00	17.00	-26.74	<
1633+39	16 33 02.1	39 24 28	1.023	16.00	15.50	...	15.40	-27.88	
2241-24	22 44 40.4	-24 03 02	1.958	16.95	16.06	16.83	16.65	16.31	15.95	15.45	14.94	-28.41	
2242-47	22 45 20.4	-47 04 50	0.201	15.28	14.22	14.95	14.64	14.13	-25.07	
2313-30	23 16 37.9	-30 29 30	0.257	15.62	15.02	15.15	14.97	14.89	-25.25	
2321-29	23 24 26.1	-28 54 59	0.279	16.44	15.84	16.03	15.80	15.35	14.75	13.93	12.90	-24.61	

Table 1—Continued

Name	R.A.(J2000)	dec(J2000)	z	m_B	m_U	m_V	m_R	m_I	m_J	m_H	m_K	M_B	P_{ra}^a
2337-33	23 39 42.7	-33 31 21	0.501	16.91	16.09	17.02	16.66	16.62	16.14	15.42	14.37	-25.36	...
2352-34	23 55 25.5	-33 57 57	0.702	16.92	15.49	16.45	16.47	16.28	-26.14	26
2357-35	0 00 01.1	-35 03 35	0.508	16.79	15.48	16.76	16.74	16.51	16.22	15.33	14.51	-25.51	...

^alog W Hz⁻¹ at 1.4GHz

Table 2. ISOPHOT Observations LOG

Source	Detector	λ (μm)	Int.time (s)	Aperture ($''$)	Chopper	RASTER
0034-70	P1	7.5	180	18	T	...
	P1	11.5	180	18	T	...
	P2	25.0	180	23	T	...
	C100	60.0	230	43.5	T	...
	C100	100.0	230	43.5	T	...
0049-29	C100	60.0	720	43.5	...	3x3
	C200	160.0	960	89.4	...	2x4
0051-39	P1	11.5	620	18	R	...
	P3	60.0	600	52	R	...
	C200	160.0	600	89.4	R	...
0059-30	P1	11.5	900	18	R	...
	P3	60.0	900	52	R	...
	C200	160.0	600	89.4	R	...
0105-26	P1	7.5	230	18	T	...
	P1	11.5	230	18	T	...
	P2	25.0	230	23	T	...
	C100	60.0	230	43.5	T	...
	C100	100.0	230	43.5	T	...
0120-28	P1	11.5	900	18	R	...
	P3	60.0	900	52	R	...
	C200	160.0	400	89.4	R	...
0129-40	C100	60.0	720	43.5	...	3x3
	C200	160.0	900	89.4	...	2x4
0144-39	C100	60.0	720	43.5	...	3x3
	C200	160.0	920	89.4	...	2x4
0203-08	P1	7.5	330	18	T	...
	P1	11.5	330	18	T	...
	P2	25.0	330	23	T	...
	C100	60.0	230	43.5	T	...
	C100	100.0	230	43.5	T	...

Table 2—Continued

Source	Detector	λ (μm)	Int.time (s)	Aperture ($''$)	Chopper	RASTER
1245-03	C100	60.0	520	43.5	...	3x3
	C200	160.0	960	89.4	...	2x4
1249-02	P3	60.0	480	52	R	...
	C200	160.0	600	89.4	R	...
1249-06	P3	60.0	330	52	R	...
	C200	160.0	360	89.4	R	...
1252+02	C100	60.0	680	43.5	...	3x3
	C200	160.0	860	89.4	...	2x4
1321-05	P3	60.0	480	52	R	...
	C200	160.0	360	89.4	R	...
1321+28	P1	7.5	200	18	T	...
	P1	11.5	200	18	T	...
	P2	25.0	200	23	T	...
	C100	60.0	230	43.5	T	...
	C100	100.0	230	43.5	T	...
1323+29	P1	7.5	230	18	T	...
	P1	11.5	230	18	T	...
	P2	25.0	230	23	T	...
	C100	60.0	230	43.5	T	...
	C100	100.0	230	43.5	T	...
1326-05	P3	60.0	270	52	R	...
	C200	160.0	150	89.4	R	...
1351+01	P1	7.5	450	18	T	...
	P1	11.5	450	18	T	...
	P2	25.0	450	23	T	...
	C100	60.0	230	43.5	T	...
	C100	100.0	230	43.5	T	...
1355+02	P3	60.0	330	52	R	...
	C200	160.0	350	89.4	R	...
1404+09	P1	7.5	180	18	T	...

Table 2—Continued

Source	Detector	λ (μm)	Int.time (s)	Aperture ($''$)	Chopper	RASTER
	P1	11.5	180	18	T	...
	P2	25.0	180	23	T	...
	C100	60.0	230	43.5	T	...
	C100	100.0	230	43.5	T	...
1406-03	P1	7.5	450	18	T	...
	P1	11.5	450	18	T	...
	P2	25.0	450	23	T	...
	C100	60.0	230	43.5	T	...
	C100	100.0	230	43.5	T	...
1415+00	P1	7.5	300	18	T	...
	P1	11.5	300	18	T	...
	P2	25.0	300	23	T	...
	C100	60.0	230	43.5	T	...
	C100	100.0	230	43.5	T	...
1415-00	P1	7.5	300	18	T	...
	P1	11.5	300	18	T	...
	P2	25.0	300	23	T	...
	C100	60.0	230	43.5	T	...
	C100	100.0	230	43.5	T	...
1424-00	P3	60.0	330	52	R	...
	C200	160.0	350	89.4	R	...
1528+28	P1	7.5	330	18	T	...
	P1	11.5	330	18	T	...
	P2	25.0	330	23	T	...
	C100	60.0	230	43.5	T	...
	C100	100.0	230	43.5	T	...
1630+37	P1	7.5	200	18	T	...
	P1	11.5	200	18	T	...
	P2	25.0	200	23	T	...
	C100	60.0	230	43.5	T	...

Table 2—Continued

Source	Detector	λ (μm)	Int.time (s)	Aperture ($''$)	Chopper	RASTER
	C100	100.0	230	43.5	T	...
1633+39	P1	7.5	180	18	T	...
	P1	11.5	180	18	T	...
	P2	25.0	180	23	T	...
	C100	60.0	250	43.5	T	...
	C100	100.0	250	43.5	T	...
2241-24	P1	11.5	900	18	R	...
	P3	60.0	900	52	R	...
	C200	160.0	600	89.4	R	...
2242-47	C100	60.0	720	43.5	...	3x3
	C200	160.0	600	89.4	...	2x4
2313-30	C100	60.0	900	43.5	...	3x3
	C200	160.0	720	89.4	...	2x4
	P1	11.5	330	18	R	...
	P3	60.0	330	52	R	...
	C200	160.0	330	89.4	R	...
2321-29	P1	11.5	900	18	R	...
	P3	60.0	900	52	R	...
	C200	160.0	600	89.4	R	...
2337-33	P1	11.5	900	18	R	...
	P3	60.0	900	52	R	...
	C200	160.0	600	89.4	R	...
2352-34	P1	11.5	900	18	R	...
	P3	60.0	900	52	R	...
	C200	160.0	600	89.4	R	...
2357-35	P1	11.5	900	18	R	...
	P3	60.0	900	52	R	...
	C200	160.0	600	89.4	R	...

Table 3. far-IR Photometry of Quasars^a

Name	F _{7μm}	F _{12μm}	F _{25μm}	F _{60μm}	F _{100μm}	F _{160μm}	F _{IRAS12}	F _{IRAS25}	F _{IRAS60}	F _{IRAS100}
0034-70	<60	<60	<90	<160	<130	...	<60	<50	<80	<210
0049-29	<105	...	<66	<60	<75	<120	<300
0051-39	...	<90	...	36±18	...	438±84	<120	<120	<150	<450
0059-30	...	<30	...	<41	...	225±74	<90	<120	<105	<360
0105-26	<100	<180	<210	<100	<140	...	<210	<120	170±40	<300
0120-28	...	<30	...	104±60	...	<300	<90	<90	180±40	240±60
0129-40	100±30	...	<90	<90	<120	<135	<300
0144-39	74±20	...	76±26	<75	<120	110±30	270±70
0203-08	<30	<60	<100	<110	<100	...	<60	<150	<150	<400
1245-03	87±22	...	50±35	<90	<240	<135	<240
1249-02	75±68	...	<90	<120	<200	<120	<300
1249-06	217±72	...	<150	<120	<150	<100	<300
1252+02	62±25	...	76±20	110±30	150±50	<90	<400
1321-05	160±50	...	<150	<100	<220	<150	<220
1321+28	<300	<300	60±25	280±130	290±95	...	<90	120±30	<110	<420
1323+29	<300	<90	<300	<110	<150	...	<120	<90	<150	<300
1326-05	160±80	...	<260	<90	<210	100±30	260±70
1351+01	<45	<90	60±20	160±60	370±130	...	<90	120±30	<90	<360
1355+02	264±78	...	<138	130±40	<105	<80	200±70
1404+09	<90	<270	70±25	380±140	566±160	...	<120	<105	<120	<360
1406-03	<45	<40	<180	310±130	546±110	...	<90	<150	<160	<600
1415+00	<45	<60	54±16	790±128	280±80	...	<135	180±40	<120	390±100
1415-00	<130	<60	56±20	475±120	190±120	...	<99	<150	140±40	280±100
1424-00	69±35	...	<120	<120	<120	<135	<210
1528+28	<60	<30	50±40	180±140	<120	...	<80	<60	<120	<220
1630+37	<45	<54	63±20	<180	150±120	...	<60	<70	<90	<270
1633+39	<200	<240	<120	<100	<100	...	<60	<75	<75	<120
2241-24	...	<24	...	45±23	...	141±83	<90	<150	<90	<240
2242-47	<62	...	<40	<90	<60	<120	<360
2313-30	...	<30	...	77±20	...	<50	90±20	<150	130±30	<600
	...			98±84		<100				

Table 3—Continued

Name	$F_{7\mu m}$	$F_{12\mu m}$	$F_{25\mu m}$	$F_{60\mu m}$	$F_{100\mu m}$	$F_{160\mu m}$	F_{IRAS12}	F_{IRAS25}	F_{IRAS60}	F_{IRAS100}
2321-29	...	<20	...	110±50	...	280±80
2337-33	...	<27	...	<36	...	<80
2352-34	...	<18	...	<33	...	<76	<90	<90	<100	<300
2357-35	...	<30	...	<30	...	290±72	140±30	<120	140±30	230±70

^aFluxes are in mJy